2D and 3D reconstructions in acousto-electric tomography

Peter Kuchment and Leonid Kunyansky

Abstract

We propose and test stable algorithms for the reconstruction of the internal conductivity of a biological object using acousto-electric measurements. Namely, the conventional impedance tomography scheme is supplemented by scanning the object with acoustic waves that slightly perturb the conductivity and cause the change in the electric potential measured on the boundary of the object. These perturbations of the potential are then used as the data for the reconstruction of the conductivity. The present method does not rely on "perfectly focused" acoustic beams. Instead, more realistic propagating spherical fronts are utilized, and then the measurements that would correspond to perfect focusing are synthesized. In other words, we use *synthetic focusing*. Numerical experiments with simulated data show that our techniques produce high quality images, both in 2D and 3D, and that they remain accurate in the presence of high-level noise in the data. Local uniqueness and stability for the problem also hold.

Introduction

Electrical Impedance Tomography (EIT) is a harmless and inexpensive imaging modality, with important clinical and industrial applications. It aims to reconstruct the internal conductivity of a body using boundary electric measurements (see, e.g., [5, 7, 9, 10]). It is well known that, regretfully, it suffers from inherent low resolution and instability. To bypass this difficulty, various versions of a new hybrid technique, sometimes called Acousto-Electric Tomography (AET), have been introduced recently [4, 8, 18, 31]. (See also [14] for a different way to recover the conductivity using combination of ultrasound and EIT). AET utilizes the electro-acoustic effect, i.e. occurrence of small changes in tissue conductivity as the result of applied acoustic pressure [22, 23]. Although the effect is small, it was shown in [31] that it provides a signal that can be used for imaging the conductivity. It has been understood [4, 8, 18] that if one could apply concentrated pressure at a given point inside the body and then measure the resulting change in impedance measurements, the knowledge of the perturbation point would have a stabilizing effect on the reconstruction in otherwise highly unstable EIT. It has been proposed to use a tightly focused ultrasound beam as a source of such point-like acoustic pressure [4]. However, since perfect focusing of acoustic waves is hard to achieve in practice (see, e.g., [16]), an alternative *synthetic focusing* approach was developed in [18]. Namely, the medium is perturbed by a series of more realistic propagating

spherical acoustic fronts with centers lying outside of the object (other options, e.g. plane waves or monochromatic spherical waves could also be used [18]). The resulting changes in the values of electric potential on the boundary of the object are recorded. Then, the data that would have been collected, if perfect focusing were possible, are synthesized mathematically. Such synthesis happens to be equivalent to the well established inversion in the so called *thermoacoustic tomography* (see, e.g., the surveys [17, 28, 30]). The results of first numerical experiments presented in [18] confirmed the feasibility of this approach.

In this article, we describe a stable and efficient local algorithm for the AET problem. From the formulas we present one can easily infer the local uniqueness and stability of the reconstruction. However, after this work was done, the authors have learned of the paper [8], some results of which (Propositions 2.1, 2.2) imply uniqueness and Lipschitz stability in the similar setting (see also [6] for the presentation of such a local result). We thus address these issues only briefly here.

The presented algorithm involves two steps. First, it synthesizes the data corresponding to perfectly focused ultrasound perturbations from the data obtained using more realistic spherical waves. Here the known smallness of the acousto-electric effect [22, 23, 31] is crucial, since it permits linearization with respect to the acoustic perturbation and thus makes synthetic focusing possible. Second, the algorithm reconstructs the conductivity from the data corresponding to perfectly focused perturbations. This second step, from measured data to the conductivity, is non-linear. We develop a linearized algorithm, assuming that the conductivity is close to a known one. The numerical examples that we provide show that this approach works surprisingly well even when the initial guess is very distinct from the correct conductivity. One can apply iterations for further improvements.

To the best of the authors' knowledge, the first step of our method (synthetic focusing) has not been discussed previously in works on AET, except for a brief description in our papers [18, 20]. On the other hand, three different approaches to reconstruction using perfectly focused beam (the second step of our algorithm) have been recently proposed [4, 8, 18, 20]. Let us thus indicate the differences with these recent works.

In [4], a single boundary current profile was used and the problem of reconstructing the conductivity was reduced to a numerical solution of a (non-linear) PDE involving the 0-Laplacian. In [18, 20], by a rather crude approximation, we reduced the reconstruction problem to solving a transport equation (a single current was used). Unfortunately, in the case of noisy measurements the errors tend to propagate along characteristics, producing unpleasant artifacts in the images, which can be reduced by iterations. There is also an elliptic version of this procedure, which works better. In [8], two current profiles are used, the problem is reduced to a minimization problem, which is then solved numerically. In the present paper we also use two (in $3D$ two or three) currents and, on the second step, use the same data as in [8]. Unlike [8], in our work the reconstruction problem is solved, under the assumption that the conductivity is close to some initial guess, by a simple algorithm, which even on the first step produces good images, improved further by iterations. The algorithm essentially boils down to solving a Poisson equation. Numerical experiments show high quality reconstructions, quite accurate even in the presence of very significant noise. Reconstructions remain accurate when the true conductivity differs significantly from the initial guess.

The rest of the paper is organized as follows: Section 1 contains the formulation of the

problem. It also addresses the focusing issue. The next Section 2 describes the reconstruction algorithm, stability of which is discussed in Section 3. Numerical implementation and results of reconstruction from simulated data in $2D$ are described in Section 4. Sections 5 and 6 are addressing the $3D$ case. Section 7 is devoted to final remarks and conclusions.

1 Formulation of the problem

Let $\sigma(x)$ be the conductivity[1] of the medium within a bounded region Ω. Then the propagation of the electrical currents through Ω is governed by the divergence equation

$$\nabla \cdot \sigma(x)\nabla u(x) = 0, x \in \Omega. \tag{1}$$

where $u(x)$ is the electric potential. Let us assume that $\sigma - 1$ is compactly supported within region Ω, and that $\sigma(x) = 1$ in the neighborhood of the boundary $\partial\Omega$. We also assume that the currents $J = \sigma\frac{\partial}{\partial n}u(x)$ through the boundary are fixed and the values of potential u are measured on the boundary $\partial\Omega$.

The acoustic wave propagating through the object slightly perturbs the conductivity $\sigma(x)$. Following the observations made in [22, 23], we assume that the perturbation is proportional to the local value of the conductivity; thus, the perturbed conductivity $\sigma^{new}(x)$ equals to $\sigma(x)\exp(\eta(x))$ where $|\eta(x)| \ll 1$ and is compactly supported. Let $u^{new}(x) = u(x) + w_\eta(x)$ be the potential corresponding to the perturbed conductivity $\sigma^{new}(x)$ and $w_\eta(x)$ be the perturbation thereof. Then, by linearizing the problem about the unperturbed solution $u(x)$, we find that $w_\eta(x)$ satisfies equation

$$\nabla \cdot \sigma(x)\nabla w_\eta(x) = -\sigma(x)\nabla u(x) \cdot \nabla\eta(x) \tag{2}$$

subject to the homogeneous Neumann boundary conditions. Since the values of $u(x)$ and $u^{new}(x)$ are measured on the boundary, the Dirichlet data for $w_\eta(x)$ are known. It will be sufficient for our purposes to measure a certain functional of the boundary values of $w_\eta(x)$. Let us fix a function $I(z)$ defined on $\partial\Omega$, and define the corresponding measurement functional $M_I(\eta)$ as follows:

$$M_{I,J}(\eta) := \int\limits_{\partial\Omega} w_\eta(z)I(z)dz. \tag{3}$$

Here the subscript J on the left reminds about the dependence of w on the current J.

The goal is to reconstruct $\sigma(x)$ from measurements of $M_{I,J}(\eta)$ corresponding to a sufficiently rich set of perturbations $\eta(x)$ in (2).

The simplest case is when one can achieve perfect focusing, and thus $\eta_y(x) \approx C\delta(x-y)$, where the point y scans through Ω. Then the reconstruction needs to be done from the values

$$M_{I,J,\delta}(y) := \int\limits_{\partial\Omega} w_{\eta_y,J}(z)I(z)dz.$$

[1] Assumptions about the conductivity that justify our considerations will be specified in Section 3.

However, this assumption of perfect focusing is unrealistic [16]. More realistic are, for instance, mono-chromatic planar or spherical waves, or short omnidirectional pulses. We chose here point-like transducers that generate such omnidirectional pulses; the corresponding acoustic pressure can be approximated as

$$\eta_{t,z}(x) := W_{t,z}(x) := \frac{\partial}{\partial t}\left(\frac{\delta(t-|x-z|)}{4\pi t}\right),$$

where z is the transducer location (outside Ω) and t is the radius of the produced spherical front[2].

The corresponding measurements then are

$$M_{I,J}(t,z) := \int\limits_{\partial\Omega} w_{W_{t,z},J}(z)I(z)dz. \tag{4}$$

Due to the linear dependence of the measurements on the acoustic perturbation η, one can try to do a "basis change" type of calculation, which would produce the "focused" data $M_{I,J,\delta}(y)$ from the more realistic "non-focused" measurements $M_{I,J}(t,z)$. In particular, as it is explained in [18, 20], if one knows the data (4) for all $t \in [0,\infty]$ and $z \in \Sigma$ (where Σ is a closed curve (surface in $3D$) surrounding Ω), then $M_{I,J,\delta}(y)$ can be reconstructed by methods of thermoacoustic tomography. In particular, if Σ is a sphere, circle, cylinder, or a surface of a cube, explicit inversion formulas exist that can recover $M_{I,J,\delta}(y)$ (see [17]). For general closed surfaces, other efficient methods exist. This transformation is known to be stable. In fact, as it will be explained below, in the version of synthetic focusing used here, it is smoothing.

We thus assume that $M_{I,J,\delta}(y)$ are known for all $y \in \Omega$, (e.g. they are obtained by synthetic focusing or by direct measurements.) For our purposes it will be sufficient to use just two functions $I_1(z), I_2(z)$ as both the current patterns and the weights in the functionals (3). We thus measure or synthesize the following values:

$$M_{i,j}(y) := \int\limits_{\partial\Omega} w_{\eta_y,I_i}(z)I_j(z)dz, \qquad i,j = 1,2.$$

We now interpret this data in a different manner. Namely, let $u_j(x)$, $j = 1,2$ be the solutions of (1) corresponding to the boundary currents (i.e., Neumann data) I_j. Then

$$\nabla\cdot\sigma(x)\nabla w_{j,\delta_y}(x) = -\sigma(y)\nabla u_j(y)\cdot\nabla\delta(x-y). \tag{5}$$

Since

$$M_{i,j} = \int\limits_{\partial\Omega} w_i(z)I_j(z)dz,$$

equation (5) and the divergence theorem lead to the formula:

$$M_{i,j}(x_0) = \sigma(x_0)\nabla u_i(x_0)\cdot\nabla u_j(x_0). \tag{6}$$

Thus, for any interior point $x \in \Omega$ and any two current profiles $I_j, j = 1,2$ on the boundary, the values of the expressions (6) can be extracted from the measured data

Our goal now is to try to recover the conductivity from these values. The same problem in $2D$ was addressed in [8], but our approach to reconstruction is different.

[2]Other "bases" of waves, e.g. radial mono-chromatic, or planar could also be used [18].

2 Reconstructing the $2D$ conductivity from focused data using two currents

We will assume here availability of the measurement data $M_{I,J}(x)$ for all $x \in \Omega$, no matter whether they were obtained by applying focused beams, or by synthetic focusing. We will consider now the situation where the conductivity $\sigma(x)$ is considered to be a (relatively) small perturbation of a known benchmark conductivity $\sigma_0(x)$:

$$\sigma(x) = \sigma_0(x)(1 + \varepsilon\rho(x)), \tag{7}$$

where $\varepsilon \ll 1$ and $\rho = 0$ near the boundary of the domain. (Numerical experiments show that our method yields quite accurate reconstructions even when the true conductivity differs significantly from the initial guess σ_0).

It will be also assumed that two distinct current patterns I_j, $j = 1, 2$ on the boundary are fixed, and the two resulting potentials $u_j, j = 1, 2$ with the benchmark conductivity σ_0:

$$\nabla \cdot \sigma_0(x)\nabla u_j(x) = 0$$

corresponding to the two prescribed sets of boundary currents. These potentials can be computed and are assumed to be known.

Correspondingly, the unknown true potentials $w_j(x) = u_j(x)+\varepsilon v_j(x)+o(\varepsilon)$ for the actual conductivity σ satisfy the equations

$$\nabla \cdot \sigma\nabla(u_j + \varepsilon v_j) = 0$$

with the same boundary currents as u_j.

According to the discussion in the previous section, using acoustic delta-perturbations (real or synthesized), we can obtain for any point x in the domain Ω the boundary voltage responses

$$M^0_{j,k}(x) := \sigma_0(x)\nabla u_j(x) \cdot \nabla u_k(x), \tag{8}$$

which can be computed numerically using the background conductivity σ_0, and

$$M_{j,k}(x) := \sigma(x)\nabla w_j(x) \cdot \nabla w_k(x) = M^0_{j,k} + \varepsilon g_{j,k} + o(\varepsilon), \tag{9}$$

which are obtained by boundary measurements. Now we can forget about the acoustic modulation and concentrate on reconstructing $\rho(x)$ (and thus $\sigma(x)$) from the known $M_{j,k}(x)$, or, neglecting higher order terms, from $g_{j,k}(x)$.

A straightforward calculation leads to the formulas

$$g_{j,k}(x) = \sigma\left(\nabla u_j \cdot \nabla v_k + \nabla u_k \cdot \nabla v_j\right) + o(\varepsilon). \tag{10}$$

We will drop the $o(\varepsilon)$ terms in the following calculations. We introduce the new vector fields $U_j = \sqrt{\sigma_0}\nabla u_j$ and $W_j = \sqrt{\sigma}\nabla(u_j + \varepsilon v_j) = U_j + \varepsilon V_j$, so that

$$\nabla \cdot \sqrt{\sigma_0}U_j = 0$$

and

$$\nabla \cdot \sqrt{\sigma}W_j = 0.$$

We would like to find W_j. The last equation can be re-written, taking into account that, up to $o(\varepsilon)$ terms, $\sqrt{\sigma} \approx \sqrt{\sigma_0}(1 + \frac{1}{2}\varepsilon\rho)$ and $\ln \sigma = \ln \sigma_0 + \varepsilon\rho$, as follows:

$$\nabla \cdot \sqrt{\sigma_0}(1 + \varepsilon\rho/2)(U_j + \varepsilon V_j) = 0$$

or

$$\nabla \cdot (U_j + \varepsilon V_j) + \frac{1}{2}(U_j + \varepsilon V_j) \cdot \nabla(\ln \sigma + \varepsilon\rho) = 0.$$

By collecting the terms of the zero and first order in ε we obtain

$$\nabla \cdot U_j + \frac{1}{2} U_j \cdot \nabla \ln \sigma = 0$$

and

$$\nabla \cdot V_j + \frac{1}{2} U_j \cdot \nabla \rho + \frac{1}{2} V_j \cdot \nabla \ln \sigma = 0$$

or

$$\nabla \cdot V_j + \frac{1}{2} V_j \cdot \nabla \ln \sigma = -\frac{1}{2} U_j \cdot \nabla \rho.$$

Equivalently

$$\nabla \cdot \sqrt{\sigma} V_j = -\frac{1}{2}\sqrt{\sigma} U_j \cdot \nabla \rho.$$

With this new notation, the measurements can be expressed (neglecting higher order terms) as follows:

$$(U_j + \varepsilon V_j) \cdot (U_k + \varepsilon V_k) = M_{j,k} = M^0_{j,k} + \varepsilon g_{j,k},$$

which leads to

$$\begin{aligned} U_j \cdot U_k &= M^0_{j,k}, \\ U_j \cdot V_k + U_k \cdot V_j &= g_{j,k}. \end{aligned}$$

In particular, we arrive to three independent equations for V_j:

$$\begin{aligned} U_1 \cdot V_1 &= g_{1,1}/2 \\ U_2 \cdot V_2 &= g_{2,2}/2 \\ U_1 \cdot V_2 + U_2 \cdot V_1 &= g_{1,2}. \end{aligned} \tag{11}$$

These equations will be our starting point for deriving reconstruction algorithms, as well as uniqueness and stability results.

We consider now the case when the benchmark conductivity (initial conductivity guess) is constant: $\sigma_0(x) \equiv 1$.

2.1 The constant benchmark conductivity $\sigma_0(x) = 1$

We will choose the boundary currents $u_j(x) = x_j$ in such a way that for the conductivity $\sigma_0 = 1$ they lead to the fields

$$U_j = \nabla u_j = e_j, j = 1, 2,$$

where $e_1 = (1, 0), e_2 = (0, 1)$ are the canonical basis vectors.

As a result, we get

$$\begin{cases} 2\frac{\partial v_1}{\partial x_1} + \rho = g_{1,1} \\ 2\frac{\partial v_2}{\partial x_2} + \rho = g_{2,2} \\ \frac{\partial v_1}{\partial x_2} + \frac{\partial v_2}{\partial x_1} = g_{1,2} \end{cases} \tag{12}$$

as well as the equations

$$\Delta v_j = -\frac{\partial}{\partial x_j}\rho, \qquad j = 1, 2. \tag{13}$$

Differentiating the equations (12), we obtain

$$\begin{cases} 2\frac{\partial^2 v_1}{\partial x_1^2} + \frac{\partial}{\partial x_1}\rho = \frac{\partial}{\partial x_1} g_{1,1} \\ 2\frac{\partial^2 v_1}{\partial x_1 \partial x_2} + \frac{\partial}{\partial x_2}\rho = \frac{\partial}{\partial x_2} g_{1,1} \\ 2\frac{\partial^2 v_2}{\partial x_2^2} + \frac{\partial}{\partial x_2}\rho = \frac{\partial}{\partial x_2} g_{2,2} \\ 2\frac{\partial^2 v_2}{\partial x_1 \partial x_2} + \frac{\partial}{\partial x_1}\rho = \frac{\partial}{\partial x_1} g_{2,2} \\ \frac{\partial^2 v_1}{\partial x_1 \partial x_2} + \frac{\partial^2 v_2}{\partial x_1^2} = \frac{\partial}{\partial x_1} g_{1,2} \\ \frac{\partial^2 v_1}{\partial x_2^2} + \frac{\partial^2 v_2}{\partial x_1 \partial x_2} = \frac{\partial}{\partial x_2} g_{1,2} \end{cases} \tag{14}$$

Combining the 2nd, 3rd, and 5th equations in (14), we arrive to

$$0 = \frac{\partial}{\partial x_2} g_{1,1} - 2\frac{\partial}{\partial x_1} g_{1,2} - \frac{\partial}{\partial x_2} g_{2,2} + 2\Delta v_2.$$

Utilizing (13) with $j = 2$ and differentiating with respect to x_2, we obtain

$$\frac{\partial^2}{\partial x_2^2}\rho = \frac{1}{2}\frac{\partial^2}{\partial x_2^2}(g_{1,1} - g_{2,2}) - \frac{\partial^2}{\partial x_1 \partial x_2} g_{1,2}.$$

Similarly,

$$\frac{\partial^2}{\partial x_1^2}\rho = \frac{1}{2}\frac{\partial^2}{\partial x_1^2}(g_{2,2} - g_{1,1}) - \frac{\partial^2}{\partial x_1 \partial x_2} g_{1,2}.$$

Adding the last two equalities, we obtain the Poisson type equation

$$\Delta\rho = \frac{1}{2}\left(\frac{\partial^2}{\partial x_1^2} - \frac{\partial^2}{\partial x_2^2}\right)(g_{2,2} - g_{1,1}) - 2\frac{\partial^2}{\partial x_1 \partial x_2} g_{1,2} \tag{15}$$

for the unknown function ρ. Notice that all expressions in the right hand side are obtained from the measured data and that by our assumption ρ satisfies the zero Dirichlet condition at the boundary.

This reduction clearly allows for algorithmic reconstruction, as well as proving (under appropriate smoothness assumptions on σ) local uniqueness and Lipschitz stability of reconstruction (see Section 3).

2.2 A parametrix solution for smooth benchmark conductivity $\sigma_0(x)$

We would like to present now a sometimes useful observation for the situation when benchmark conductivity σ_0 is smooth, but not necessarily constant (e.g., a standard EIT reconstruction would provide such an approximation). In this case, we will find a parametrix solution, i.e. will determine $\sigma(x)$ up to smoother terms.

As it has already been discussed, perturbation εv_j of the potential u_j satisfies the equation

$$\nabla \cdot \sigma_0 \nabla v_j = -\sigma_0 \nabla u_j \cdot \nabla \rho.$$

Since σ is smooth and non-vanishing, up to smoother terms we can write

$$\Delta v_j \approx -\nabla u_j \cdot \nabla \rho$$

and

$$v_j \approx -(\nabla u_j \cdot \nabla)(\Delta^{-1}\rho)$$

where Δ^{-1} is the inverse to the Dirichlet Laplacian in Ω. Again up to smoother terms, we have

$$\begin{aligned} U_k \cdot V_j &= \sqrt{\sigma}\nabla u_k \cdot \sqrt{\sigma}(\rho/2\nabla u_j + \nabla v_j) \\ &= \sigma\rho/2\nabla u_k \cdot \nabla u_j + \sigma(\nabla u_k \cdot \nabla)(\nabla u_j \cdot \nabla)\Delta^{-1}\rho. \end{aligned}$$

The latter expression is symmetric up to smoothing terms and equations (11) can be re-written as

$$\begin{aligned} &U_1 \cdot V_1 = g_{1,1}/2 \\ &U_2 \cdot V_2 = g_{2,2}/2 \\ &U_1 \cdot V_2 = g_{1,2}/2 + \text{ a smoother term} \\ &U_2 \cdot V_1 = g_{1,2}/2 + \text{ a smoother term.} \end{aligned}$$

Under such an approximation, assuming that currents ∇u_1 and ∇u_2 are not parallel, which is known to be possible to achieve [2], one can recover εV_j at each point x. Therefore, (more) accurate solutions $W_j = U_j + \varepsilon V_j$ can be found. We note that $\nabla \cdot \sqrt{\sigma} W_j = 0$ and so

$$W_j \cdot \nabla \ln \sigma = -2\nabla \cdot W_j.$$

On the other hand, since $W_j = \sqrt{\sigma}\nabla(u_j + \varepsilon v_j)$, we have

$$\nabla \times \frac{W_j}{\sqrt{\sigma}} = 0.$$

This can be re-written as

$$W_j \times \nabla \ln \sigma = -2\nabla \times W_j$$

or

$$W_j^{\perp} \cdot \nabla \ln \sigma = -2\nabla \times W_j,$$

where $W_j^\perp$ is the vector obtained from W_j by the counter-clockwise 90^o rotation (i.e. $W_j^\perp \cdot W_j = 0$ and $|W_j^\perp| = |W_j|$).

Since for each $j = 1, 2$ vectors W_j and $W_j^\perp$ form an orthogonal basis, one has

$$\nabla \ln \sigma = -\frac{2}{|W_j|^2}(W_j^\perp(\nabla \times W_j) + W_j(\nabla \cdot W_j)),$$

and thus

$$\Delta \ln \sigma = -\operatorname{div} \frac{2}{|W_j|^2}(W_j^\perp(\nabla \times W_j) + W_j(\nabla \cdot W_j)).$$

We compute now $\ln \sigma$ by taking the average of the two values of j and then solving the Poisson equation

$$\Delta \ln \sigma = -\operatorname{div} \sum_{j=1}^{2} \frac{2}{|W_j|^2}(W_j^\perp(\nabla \times W_j) + W_j(\nabla \cdot W_j)).$$

It is interesting to note that this solution reduces to (15) when $\sigma = 1$, although (15) holds exactly, not just up to smoother terms.

3 Uniqueness and stability

In this section we will assume that $\sigma \in C^{1,\alpha}(\Omega)$, and thus ρ belongs to this space as well (recall that ρ also vanishes in a fixed neighborhood of $\partial\Omega$).

The questions of uniqueness and stability in the situation close to ours have already been addressed in [6, 8], so we will be brief here. Although considerations of [6, 8] were provided in $2D$, the conclusion in our situation works out the same way in $3D$.

The standard elliptic regularity [15] implies

Proposition 1 *[6, 8]*

1. *The data $g_{i,j}$ in (9) determine the conductivity $\sigma = 1 + \rho$ uniquely.*
2. *The mappings $\rho(x) \mapsto \{g_{i,j}(x)\}$ of the space $C_0^{1,\alpha}(\overline{V})$, where V is a compact sub-domain of Ω, are Fréchet differentiable.*

This justifies our formal linearization near the benchmark conductivity σ_0. Now, the calculations of the Section 2.1 provide explicit formulas for the Fréchet derivative of the proposition[3]. In particular,

$$\begin{array}{l} \frac{\partial}{\partial x_1}\rho = \frac{1}{2}\frac{\partial}{\partial x_1}(g_{2,2} - g_{1,1}) - \frac{\partial}{\partial x_2}g_{1,2}, \\ \frac{\partial}{\partial x_2}\rho = \frac{1}{2}\frac{\partial}{\partial x_2}(g_{1,1} - g_{2,2}) - \frac{\partial}{\partial x_1}g_{1,2}. \end{array} \tag{16}$$

These formulas and vanishing of ρ near $\partial\Omega$ show that the norm of ρ in $C^{1,\alpha}$ can be estimated from above by such norms of the functions $\{g_{11}, g_{12}, g_{22}\}$. In other words, the Fréchet derivative of the mapping

$$\rho \mapsto \{g_{11}, g_{12}, g_{22}\} \tag{17}$$

[3]In fact, these formulas easily imply the statement of the proposition in our particular case.

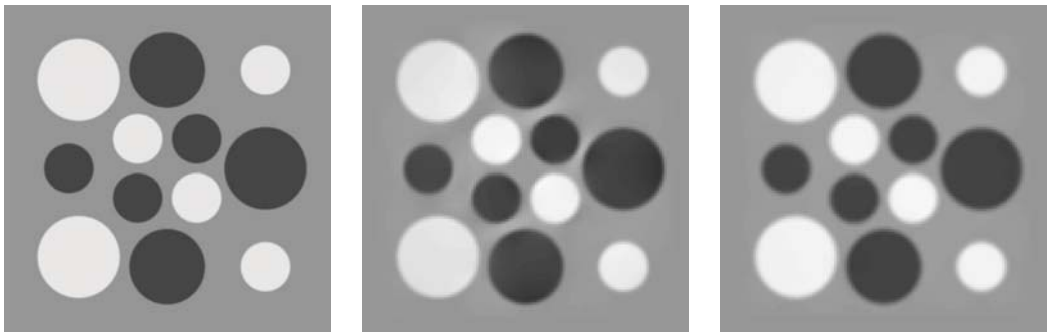

(a) (b) (c)

Figure 1: Reconstruction in $2D$ from noiseless data (a) phantom (b) iteration #0 (c) iteration #1

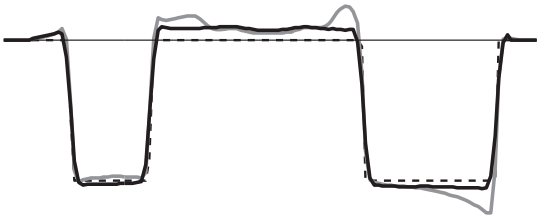

Figure 2: Horizontal central cross-section (accurate data): dashed line denotes the phantom, gray line represents iteration # 0, thick black solid line represents iteration #1

is a semi-Fredholm operator with zero kernel. Then the standard implicit function type argument shows (see, e.g., [21, Corollary 5.6, Ch. I]) that (17) is an immersion.

This proves local uniqueness and stability for the non-linear problem (analogous result is obtained in $2D$ in [6]). The $3D$ case works the same way.

Moreover, since our algorithms start with inverting the Fréchet derivative, this reduces near the constant conductivity the non-linear problem to the one with an identity plus a contraction operator. This explains why the fixed point iterations in the following sections converge so nicely.

4 Numerical examples in $2D$

We will now illustrate the properties of our algorithm on several numerical examples in $2D$.

As the first step, in order to simulate the measurements, one needs to have a very precise forward solver. The reason is that, due to the smallness of the acousto-electric effect, the AET data comes from minute perturbations of the boundary measurements. We thus carefully simulate the direct problem by using a pseudospectral algorithm and by performing computations on a fine mesh 512×512. We also would like to note that no linearization is used in the forward simulations (which, in particular, eliminates the chance of committing

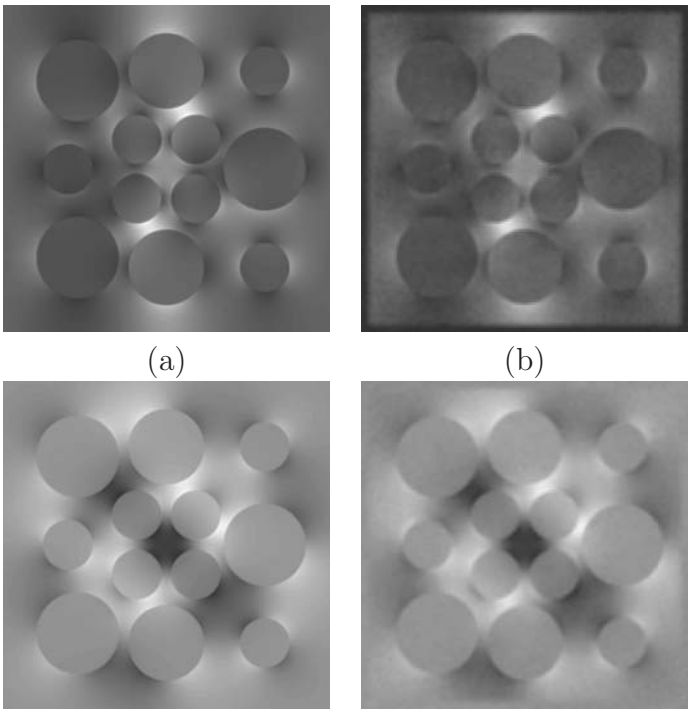

(a) (b)

(c) (d)

Figure 3: Functionals $M_{i,j}$: (a) original $M_{1,1}$ (b) $M_{1,1}$ reconstructed from data contaminated by 50% noise (c) original $M_{1,2}$ (d) $M_{1,2}$ reconstructed from data contaminated by 50% noise

an inverse crime).

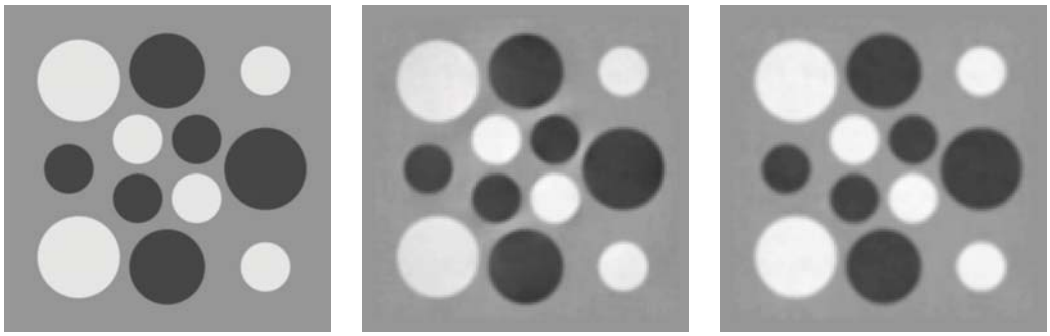

(a) (b) (c)

Figure 4: Reconstruction from the data contaminated by a 50% noise (a) phantom (b) iteration #0 (c) iteration #1

For simplicity, as the reconstruction domain we used the unit square $[-1,1] \times [-1,1]$. Our phantom (i.e., simulated $\ln \sigma(x)$) consists of several slightly smoothed characteristic functions of circles, shown in Figure 1(a) and Figure 4(a). Smoothing guarantees that the phantom is fully resolved on the fine grid during the forward computations, which helps

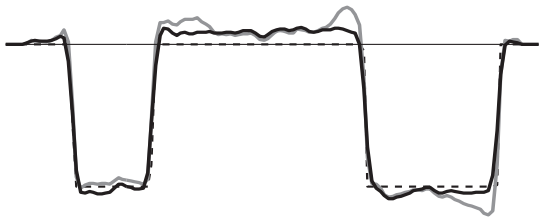

Figure 5: Horizontal central cross-section (noisy data): dashed line denotes the phantom, gray line represents iteration #0, thick black solid line represents iteration #1

to ensure its high accuracy (several correct decimal digits). The characteristic functions comprising the phantom are weighted with weights 1 or -1, so that $\sigma(x)$ varies between e and e^{-1}. Thus, the conductivity deviates far from the initial guess $\sigma_0 \equiv 1$. Current I_1 equals 1 and -1 on the right and left sides of square, respectively; it vanishes on the horizontal sides. Current I_2 coincides with I_1 rotated 90 degrees counterclockwise.

The simulated sources of the propagating spherical acoustic fronts are centered on a circle of the diameter slightly larger than the diagonal of the square domain. There were 256 simulated transducers uniformly distributed over the circle. Each transducer produced 257 spherical fronts of the radii ranging from 0 to the diameter of the circle. For each front radius t_l and center z_m, the perturbed σ was modeled, the non-linear direct problem was solved, and the values of the functionals $M_{I_j,I_k}(t_l, z_m)$, $j, k = 1, 2$ were computed. In the first of our experiments, these accurate data were used as a starting point of the reconstruction. In the second experiment, they were perturbed by a 50% (in the L^2 norm) noise.

(a) (b) (c)

Figure 6: Reconstruction from noiseless data (a) phantom (b) iteration #0 (c) iteration #4

As explained in the previous sections, the first step of the reconstruction is synthetic focusing, i.e. finding the values $M_{j,k}(x)$ from $M_{I_j,I_k}(t, z)$, $j, k = 1, 2$. This was done using the $2D$ exact filtration backprojection formula from [19] (although other options are also available). On a 129×129 grid this computation takes a few seconds. Since the formula is applied to the data containing the derivative of the delta-function, the differentiation appearing in the TAT inversion formula (e.g., [1, 12, 17, 19]) is not needed, and the reconstruction instead

of being slightly unstable, has a smoothing effect (this is why we obtain high quality images with such high level of noise).

On the second step of the reconstruction, functions $M^0_{j,k}(x)$ are computed using the knowledge of the benchmark conductivity σ_0, and values of $g_{j,k}(x)$ are obtained by comparing $M_{j,k}(x)$ and $M^0_{j,k}(x)$. Then the first approximation to ρ (we will call it iteration #0) is obtained by solving equation (15). The right hand side of this equation is computed by finite differences, and then the Poisson equation in a square is solved by the decomposition in 2D Fourier series. The computation is extremely fast due to the use of the FFT. More importantly, since the differentiation of the data is followed by the application of the inverse Laplacian, this step is completely stable (the corresponding pseudodifferential operator is of order zero), and no noise amplification occurs.

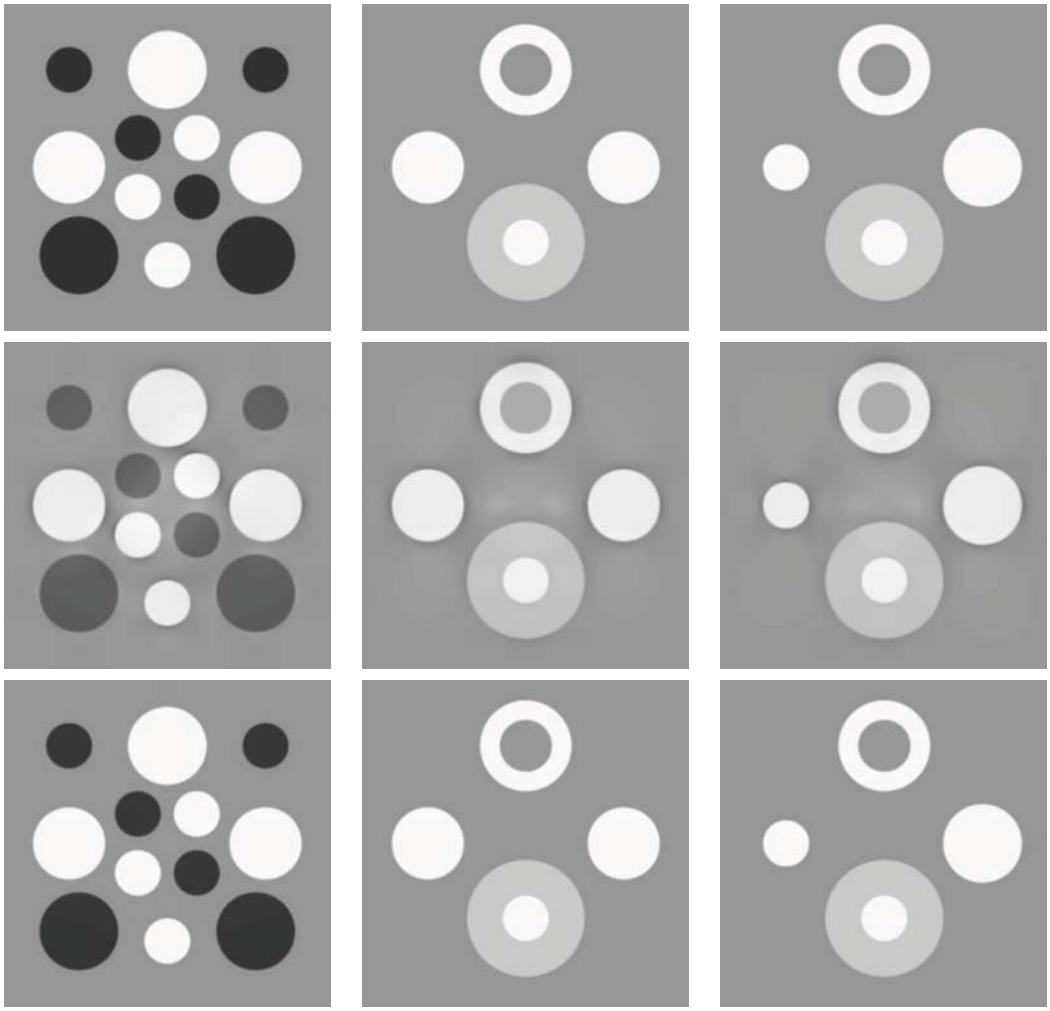

(a) (b) (c)

Figure 7: 3D Reconstruction from noiseless data. First row: phantom (a) Oxy cross section (b) Oxz cross section (c) Oyz cross section. Second row: iteration #0; Third row: iteration #4

Finally, we attempt to improve the reconstruction by accepting the reconstructed σ as a

new benchmark conductivity and by applying to the data the parametrix algorithm of the previous section. We will call this computation iteration #1.

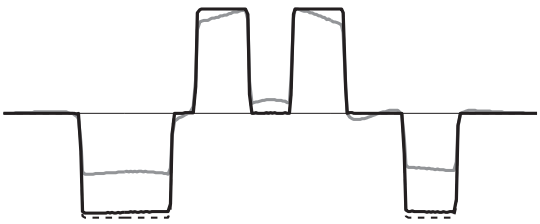

Figure 8: Diagonal cross-section (noiseless data): dashed line denotes the phantom, gray line represents iteration # 0, thick black solid line represents iteration #4

Figure 1 demonstrates the result of such reconstruction from accurate data. Part (a) of the Figure shows the phantom, parts (b) and (c) present the results of iterations #0 and #1, on the same gray-level scale. The profiles of the central horizontal cross-sections of these functions are shown in Figure 2. One can see that even the iteration #0 produces quite good a reconstruction; iteration #1 removes some of the artifacts, and improves the shape of circular inclusions.

Figures 3, 4 and 5 present the results of the reconstruction from noisy data. In his simulation we used the phantom from the previous example, and we added to the data 50% (in L^2 norm) noise. The first step of the reconstruction (synthetic focusing) is illustrated by Figure 3. Parts (a) and (c) of this Figure show accurate values of the functionals $M_{1,1}(x)$ and $M_{1,2}(x)$. Parts (b) and (d) present the reconstructed values of these functionals obtained by synthetic focusing. One can see the effect of smoothing mentioned earlier in this section: the level of noise in the reconstructions is much lower than the level of noise in the simulated measurements. The images reconstructed from $M_{i,j}(x)$ on the second step are presented in Figures 4 and 5 The meaning of the images is the same as of those in Figures 1 and 2. The level of noise in these images is comparable to that in the reconstructed $M_{i,j}$'s. To summarize, our method can reconstruct high quality images from the data contaminated by a strong noise since the first step of the method is an application of a smoothing operator, and the second step uses the parametrix.

Finally, Figure 6 shows reconstruction of a phantom containing objects with corners. The phantom is shown in the part (a) of the figure, part (b) demonstrates iteration #0, and part (c) presents the result of the iterative use of the parametrix method described in the previous section (iteration #4 is shown).

5 Reconstruction in $3D$

Let us now consider the reconstruction problem in $3D$. The $3D$ case is very important from the practical point of view, since propagation of electrical currents is essentially three-dimensional. Indeed, unlike X-rays or high-frequency ultrasound, currents cannot be focused to stay in a two-dimensional slice of the body. However, it looks like the $3D$ case has not been addressed in the literature yet, due to some analytic difficulties arising in other approaches.

In contrast, the present approach easily generalizes to $3D$, and leads to a fast, efficient, and robust reconstruction algorithm.

We will assume that three different currents $I_j, j = 1, 2, 3$ are used, and that the boundary values of the corresponding potentials w_j, $j = 1, 2, 3$ are measured on $\partial\Omega$. Similarly to the $2D$ case presented in Section 1, by perturbing the medium with a perfectly focused acoustic beam (no matter whether such measurements are real or synthesized) one can recover at each point x within Ω the values of the functionals $M_{i,j}(x)$, $i, j = 1, 2, 3$, where, as before,

$$M_{i,j}(x) = \sigma(x)\nabla w_i(x) \cdot \nabla w_j(x).$$

Our goal is to reconstruct conductivity $\sigma(x)$ from $M_{i,j}(x)$. As before, we will assume that $\sigma(x)$ is a perturbation of a known benchmark conductivity $\sigma_0(x)$, i.e. $\sigma(x) = \sigma_0(x)(1+\varepsilon\rho(x))$, and that the values of potentials $w_j(x)$ are the perturbations of known potentials $u_j(x)$ corresponding to $\sigma_0(x)$:

$$w_j(x) = u_j(x) + \varepsilon v_j(x) + o(\varepsilon).$$

Now functionals $M_{j,k}(x)$ are related to the known unperturbed values $M^0_{j,k}(x)$ and measured perturbations $g_{j,k}(x)$ by equations (9) and (8).

As it was done in Section 2, we introduce vector fields $U_j = \sqrt{\sigma_0}\nabla u_j$ and $W_j = \sqrt{\sigma}\nabla(u_j + \varepsilon v_j) = U_j + \varepsilon V_j$, and proceed to derive the following six equations:

$$\begin{aligned}
U_1 \cdot V_1 &= g_{1,1}/2 \\
U_2 \cdot V_2 &= g_{2,2}/2 \\
U_3 \cdot V_3 &= g_{3,3}/2 \\
U_1 \cdot V_2 + U_2 \cdot V_1 &= g_{1,2} \\
U_1 \cdot V_3 + U_3 \cdot V_1 &= g_{1,3} \\
U_2 \cdot V_3 + U_3 \cdot V_2 &= g_{2,3}.
\end{aligned}$$

One can obtain a useful approximation to $\rho(x)$ by assuming $\sigma_0 = 1$, and by selecting unperturbed currents so that the potentials $u_j(x) = x_j$. Then, by repeating derivations of Section 2.1 one obtains the following three formulas

$$\left\{ \begin{array}{l}
\left(\frac{\partial^2}{\partial x_1^2} + \frac{\partial^2}{\partial x_2^2}\right)\rho = \frac{1}{2}\left(\frac{\partial^2}{\partial x_1^2} - \frac{\partial^2}{\partial x_2^2}\right)(g_{2,2} - g_{1,1}) - 2\frac{\partial^2}{\partial x_1 \partial x_2} g_{1,2} \\
\left(\frac{\partial^2}{\partial x_1^2} + \frac{\partial^2}{\partial x_3^2}\right)\rho = \frac{1}{2}\left(\frac{\partial^2}{\partial x_1^2} - \frac{\partial^2}{\partial x_3^2}\right)(g_{3,3} - g_{1,1}) - 2\frac{\partial^2}{\partial x_1 \partial x_3} g_{1,3} \\
\left(\frac{\partial^2}{\partial x_2^2} + \frac{\partial^2}{\partial x_3^2}\right)\rho = \frac{1}{2}\left(\frac{\partial^2}{\partial x_2^2} - \frac{\partial^2}{\partial x_3^2}\right)(g_{3,3} - g_{2,2}) - 2\frac{\partial^2}{\partial x_2 \partial x_3} g_{2,3}
\end{array} \right. \tag{18}$$

We notice that by using the first of the above equations one can compute an approximation to $\rho(x)$ by solving a set of $2D$ Poisson equations (one for each fixed value of x_3), since boundary values of $\rho(x)$ are equal to 0. This leads to a slice-by-slice $3D$ reconstruction, which is based only on values of $g_{1,1}$, $g_{2,2}$ and $g_{1,2}$, and therefore can be done by using a single pair of currents.

One can get better images by using all three currents and doing a fully $3D$ reconstruction. Namely, summing the equations (18) yields the values of $2\Delta\rho$ in the left hand side. Then one can solve the $3D$ Poisson equation with the zero boundary conditions to recover the conductivity.

One can expect that, as in $2D$, this approach would work well for $\sigma(x)$ close to $\sigma_0 = 1$. However, as demonstrated by our numerical experiments presented in Section 6, the results remain quite accurate when $\sigma(x)$ varies significantly across Ω. Moreover, a simple fixed point iteration based on the repeated use of formulas (18) exhibits a rapid convergence to the correct image.

6 Numerical examples in $3D$

In this section we present results of $3D$ reconstructions from simulated data. Unfortunately, a complete modeling of the forward problem in $3D$ (i.e. computation of the perturbations corresponding to the propagating acoustic spherical fronts) would require solution of $\mathcal{O}(n^3)$ $3D$ divergence equations. This task is computationally too expensive. Therefore, unlike in our $2D$ simulations, we resort to modeling the values of the functionals $M_{i,j}(x)$ on a $257 \times 257 \times 257$ Cartesian grid, using formulas (5). These values correspond to the data that would be measured if perfectly focused, infinitely small perturbations were applied to the conductivity. Thus, in this section we only test the second step of our reconstruction techniques. However, as mentioned before, if the real data were available, the first step (synthetic focusing) could be done by applying any of the several available stable versions of thermoacoustic inversion, and the feasibility of this step was clearly demonstrated in the $2D$ sections of this paper, as well as in [18].

In our first simulation we used noiseless values of $M_{i,j}(x)$ and reconstructed the conductivity on a $257 \times 257 \times 257$ grid. The first row of Figure 7 shows three $2D$ cross-sections of a $3D$ phantom. The result of approximate inversion (using three currents, as described in Section 5) is presented in the second row of the figure. Finally, the last row shows the result of iterative use of formulas (18), where ρ now represents the difference between the previous and the updated approximations to the conductivity. The third row demonstrates iteration #4. In addition, Figure 8 shows the trace along a diagonal cross section in Oxy plane (that corresponds to the diagonals of images presented in the column (a) of Figure 7).

In our second $3D$ experiment we utilized the same phantom, but as a data used only a subset of the values of $M_{i,j}$ corresponding to a coarser $129 \times 129 \times 129$ grid; the latter coarse grid was also used to discretize the reconstructed conductivity. We also added to the data a 10% (in L^2 norm) noise. Figure 9 presents the cross-sections of a $3D$ phantom and the reconstructions obtained using three currents, on the same gray-level scale. The meaning of the subfigures is the same as of those in Figure 7. Finally, Figure 10 shows the trace along the diagonal cross sections of the images in the Oxy plane.

In both these examples iteration #0 yields good qualitative reconstruction of the conductivity in spite the fact that the latter varies from e^{-1} to e^1, and thus differs strongly from the benchmark guess $\sigma_0 = 1$. The subsequent iterations demonstrate fast convergence to the correct values of $\sigma(x)$.

7 Final remarks and conclusions

We have shown that the proposed algorithm works stably and yields quality reconstructions of the internal conductivity. It does not require physical focusing of ultrasound waves and

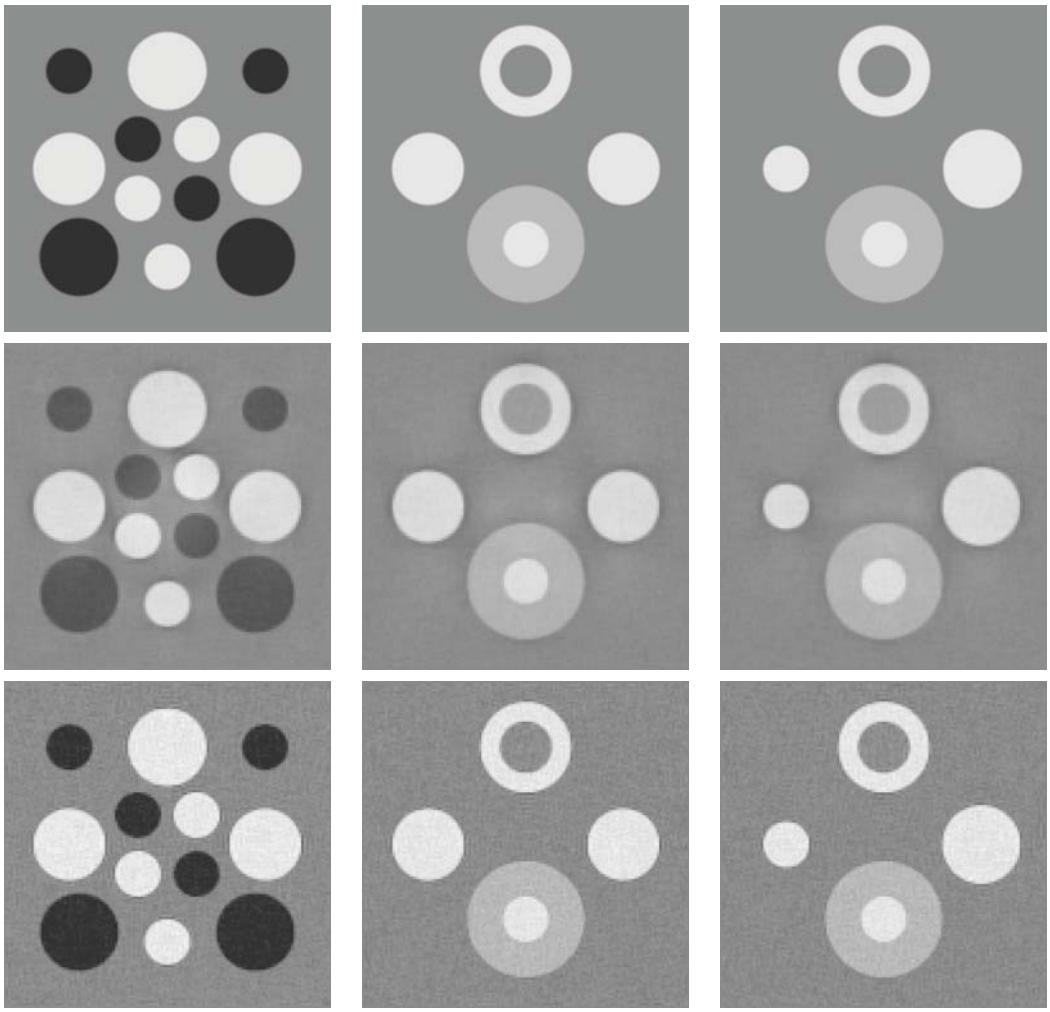

Figure 9: 3D Reconstruction from noisy data on a coarser grid. First row: phantom (a) Oxy cross section (b) Oxz cross section (c) Oyz cross section. Second row: iteration #0; Third row: iteration #4

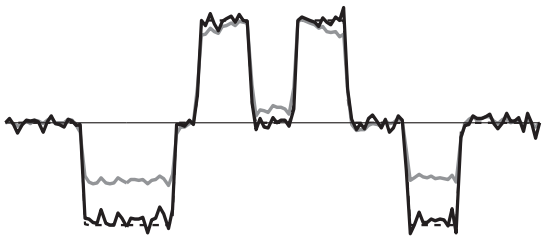

Figure 10: Diagonal cross-section of reconstructions obtained from noisy data on a coarser gird: dashed line denotes the phantom, gray line represents iteration # 0, thick black solid line represents iteration #4

replaces it with the synthetic focusing procedure, which can be implemented using one of the known thermoacoustic imaging inversion methods (e.g., time reversal or inversion formulas). Under appropriate smoothness conditions on the conductivity, our analysis leads to the proof of local uniqueness and stability of the reconstruction. However, since this conclusion has been already made in $2D$ in [6, 8], we only presented a sketch of the proof.

Some additional remarks:

1. Using the spherical waves of the type considered in this text (which approximate an omnidirectional short spherical pulse from a point-like transducer) has the advantage that the synthetic focusing is a smoothing operator, and thus the whole reconstruction procedure is more stable with respect to errors than the one that starts with focused data.

2. Reconstructions can be done with a single, two, or (in $3D$) three currents. A single current procedure was the one we used initially in $2D$. It works, but requires solving a transport equation for the conductivity. When such a procedure is used, errors arising due to the noise and/or underresolved interfaces tend to propagate along the current lines, thus reducing the quality of the reconstructed image. The two-current approach in $2D$ is elliptic and thus does not propagate errors. The two-current slice-by-slice reconstruction in $3D$ is also possible, but the use of three currents seem to produce better results.

The results of this work were presented at the conferences "Integral Geometry and Tomography", Stockholm, Sweden, August 2008; "Mathematical Methods in Emerging Modalities of Medical Imaging", BIRS, Banff, Canada, October, 2009; "Inverse Transport Theory and Tomography", BIRS, Banff, May 2010; "Mathematics and Algorithms in Tomography" Oberwolfach (April 2010), and "Inverse problems and applications", MSRI, Berkeley, August 2010. The brief reports have appeared in [18, 20].

Acknowledgments

The work of both authors was partially supported by the NSF DMS grant 0908208; the manuscript was written while they were visiting MSRI. The work of P. K. was also partially supported by the NSF DMS grant 0604778 and by KAUST through the IAMCS. The authors express their gratitude to NSF, MSRI, KAUST, and IAMCS for the support. Thanks also go to G. Bal, E. Bonnetier, J. McLaughlin, L. V. Ngueyn, L. Wang, and Y. Xu for helpful discussions and references.

References

[1] M. Agranovsky, P. Kuchment, and L. Kunyansky, *On reconstruction formulas and algorithms for the thermoacoustic and photoacoustic tomography*, Ch. 8 in L. H. Wang (Editor) "Photoacoustic imaging and spectroscopy," CRC Press 2009, pp. 89-101.

[2] G. Alessandrini and V. Nesi, Univalent σ-harmonic mappings, Arch. Ration. Mech. Anal., **158** (2001), 155—171.

[3] H. Ammari, "An Introduction to Mathematics of Emerging Biomedical Imaging", Springer-Verlag, 2008.

[4] H. Ammari, E. Bonnetier, Y. Capdeboscq, M. Tanter, and M. Fink, *Electrical impedance tomography by elastic deformation*, SIAM J. Appl. Math. **68** (2008), 1557–1573.

[5] D. C. Barber, B. H. Brown, *Applied potential tomography*, J. Phys. E.: Sci. Instrum. **17**(1984), 723–733.

[6] E. Bonnetier and F. Triki, A stability result for electric impedance tomography by elastic perturbation, Presentation at the workshop "Inverse Problems: Theory and Applications", November 12th, 2010. MSRI, Berkeley, CA.

[7] L. Borcea, *Electrical impedance tomography*, Inverse Problems **18** (2002), R99–R136.

[8] Y. Capdeboscq, J. Fehrenbach, F. de Gournay, O. Kavian, Imaging by modification: numerical reconstruction of local conductivities from corresponding power density measurements, SIAM J. Imaging Sciences, **2/4** (2009), 1003–1030.

[9] M. Cheney, D. Isaacson, and J.C. Newell, Electrical Impedance Tomography, SIAM Review, 41, No. 1, (1999), 85–101.

[10] B. Cipra, Shocking images from RPI, SIAM News, July 1994, 14–15.

[11] D. Finch, S. Patch, and Rakesh, *Determining a function from its mean values over a family of spheres*, SIAM J. Math. Anal. **35** (2004), no. 5, 1213–1240.

[12] D. Finch and Rakesh, *The spherical mean value operator with centers on a sphere*, Inverse Problems **23** (2007), S37–S50.

[13] D. Finch and Rakesh, *Recovering a function from its spherical mean values in two and three dimensions*. In L. H. Wang (Editor) "Photoacoustic imaging and spectroscopy," CRC Press 2009, pp. 77–88.

[14] B. Gebauer and O. Scherzer, *Impedance-Acoustic Tomography*, SIAM J. Applied Math. **69**(2): 565-576, 2009.

[15] D. Gilbarg and N. S. Trudinger, *Elliptic partial differential equations of second order*, Reprint of the 1998 edition, Classics in Mathematics, Springer-Verlag, Berlin, 2001.

[16] H. E. Hernandez-Figueroa, M. Zamboni-Rached, and E. Recami (Editors), "Localized Waves", IEEE Press, J. Wiley & Sons, Inc., Hoboken, NJ 2008.

[17] P. Kuchment and L. *Kunyansky, Mathematics of thermoacoustic tomography*, European J. Appl. Math., **19** (2008), Issue 02, 191–224.

[18] P. Kuchment and L. Kunyansky, Synthetic focusing in ultrasound modulated tomography, Inverse Problems and Imaging, **4** (2010), Number 4, 665 – 673.

[19] L. A. Kunyansky, *Explicit inversion formulae for the spherical mean Radon transform*, Inverse Problems **23** (2007), pp. 373–383.

[20] L. Kunyansky and P. Kuchment, Synthetic focusing in Acousto-Electric Tomography, in *Oberwolfach Report* No. 18/2010 DOI: 10.4171/OWR/2010/18, Workshop: Mathematics and Algorithms in Tomography, Organised by Martin Burger, Alfred Louis, and Todd Quinto, April 11th – 17th, 2010, pp. 44-47.

[21] S. Lang, *Introduction to Differentiable Manifolds*, 2nd edition, Springer Verlag, NY 2002.

[22] B. Lavandier, J. Jossinet and D. Cathignol, *Quantitative assessment of ultrasound-induced resistance change in saline solution*, Medical & Biological Engineering & Computing **38** (2000), 150–155.

[23] B. Lavandier, J. Jossinet and D. Cathignol, *Experimental measurement of the acousto-electric interaction signal in saline solution*, Ultrasonics **38** (2000), 929–936.

[24] J. Li and L.-H. Wang, *Methods for parallel-detection-based ultrasound-modulated optical tomography*, Applied Optics **41** (2002), 2079–2084.

[25] H. Nam. "Ultrasound modulated optical tomography", Ph.D thesis, Texas A&M University, 2002.

[26] H. Nam and D. Dobson, *Ultrasound modulated optical tomography*, preprint 2004.

[27] Linh V. Nguyen, A family of inversion formulas in thermoacoustic tomography, Inverse Probl. Imaging, **3**(4): 649-675, 2009.

[28] L. V. Wang and H. Wu, "Biomedical Optics. Principles and Imaging", Wiley-Interscience 2007.

[29] M. Xu and L.-H. V. Wang, *Universal back-projection algorithm for photoacoustic computed tomography*, Phys. Rev. E **71** (2005), 016706.

[30] M. Xu and L.-H. V. Wang, *Photoacoustic imaging in biomedicine*, Review of Scientific Instruments **77** (2006), 041101-01 – 041101-22.

[31] H. Zhang and L. Wang, *Acousto-electric tomography*, Proc. SPIE 5320 (2004), 145–149.